RSC Advances

PAPER

View Article Online
View Journal | View Issue

Cite this: *RSC Adv.*, 2025, **15**, 8060

First-principles study of $Ga_2Ge_2S_3Se_3$ monolayer: a promising photocatalyst for water splitting†

Pham D. Trung *[a] and Hien D. Tong [b]

Recently, the quaternary Janus monolayers with the formula $A_2B_2X_3Y_3$ have been shown to be promising candidates for optoelectronic applications, especially in the photocatalytic water splitting reaction. Therefore, first-principles calculations were employed to investigate the photocatalytic properties of $Ga_2Ge_2X_3Y_3$ (X and Y represent S, Se or Te atoms) monolayers. The $Ga_2Ge_2S_3Se_3$ and $Ga_2Ge_2Se_3Te_3$ monolayers exhibit dynamic and thermal stability, supported by high cohesive energies (3.78–4.20 eV) and positive phonon dispersion. With a moderate Young's modulus (50.02–65.31 N m^{-1}) and high Poisson's ratio (0.39–0.41), these monolayers offer a balance of stiffness and flexibility, making them suitable for flexible electronic applications. Especially, the difference in work function of 0.27 eV induces an intrinsic electric field in the $Ga_2Ge_2S_3Se_3$ monolayer, making the electronic structure of this material be suitable for the photocatalytic water splitting process. With light irradiation, the oxygen evolution reaction (OER) happened simultaneously, producing electrons and H^+ protons for the hydrogen evolution reaction (HER) to happen at a low potential barrier. Moreover, the $Ga_2Ge_2S_3Se_3$ monolayer has a high absorption rate $\alpha(\omega)$ of 10^5–10^6 cm^{-1} and a high electron mobility of 430.82–461.50 cm^2 V^{-1} s^{-1}. These characteristics result in a good solar-to-hydrogen η'_{STH} of the $Ga_2Ge_2S_3Se_3$ monolayer (14.80%) which is promising for use in photon-driven water splitting.

Received 3rd February 2025
Accepted 9th March 2025

DOI: 10.1039/d5ra00812c

rsc.li/rsc-advances

1 Introduction

Water splitting, the process of decomposing water into hydrogen and oxygen through electrolysis, offers a potential solution to the global energy crisis. This technology holds the promise of a clean, sustainable, and efficient energy future. A variety of materials have been explored as photocatalysts for water splitting, each with its unique properties and potential advantages. Inorganic semiconductors, such as metal oxides (TiO_2, ZnO, Fe_2O_3),[1–3] metal sulfides (CdS, ZnS),[4,5] and metal nitrides (TiN),[6] have been extensively studied. While these materials offer stability and high catalytic activity, their performance is often limited by factors like wide bandgaps and rapid charge carrier recombination. Organic semiconductors, including graphitic carbon nitride (g-C_3N_4) and organic dyes,[7,8] offer advantages such as low cost and tunable bandgaps. However, their stability and efficiency can be compromised. Hybrid materials, combining the best of both inorganic and organic worlds, have emerged as promising candidates.[9] These materials often exhibit enhanced light absorption, charge separation, and stability.

To further enhance the efficiency of photocatalytic water splitting, researchers are exploring various strategies. Bandgap engineering, which involves modifying the bandgap of materials to better match the solar spectrum, is a key approach. Additionally, strategies to prevent electron–hole recombination, such as introducing co-catalysts or forming heterojunctions, are being investigated.[3,10] Surface modification techniques are employed to improve light absorption and charge transfer, while nanostructuring is used to increase surface area and light harvesting efficiency.[4,5] These advancements hold the potential to significantly improve the performance of photocatalytic water splitting systems.

Among 2D materials, ternary 2D chalcogenides have emerged as promising materials for photocatalytic water splitting due to their unique electronic and optical properties.[11] Compounds like $ZnIn_2S_4$ and $AgInS_2$ have garnered significant attention.[12] These materials often exhibit suitable bandgap energies for visible light absorption, efficient charge carrier separation, and enhanced stability compared to their binary counterparts.[13] However, challenges such as photocorrosion and low carrier mobility still need to be addressed. Ongoing research focuses on optimizing synthesis techniques, incorporating co-catalysts, and developing heterostructures to further improve the photocatalytic performance of these materials.

Two-dimensional (2D) layered transition metal phosphorus trichalcogenides (MPX_3, where M represents transition metals and X = S, Se) exhibit high in-plane stiffness and lower cleavage

[a]*Yersin University, 27 Ton That Tung, Ward 8, Dalat City, Lam Dong Province, Vietnam. E-mail: phdtrung2018@gmail.com*

[b]*Faculty of Engineering, Vietnamese-German University (VGU), Ben Cat City, Binh Duong Province, Vietnam*

† Electronic supplementary information (ESI) available. See DOI: https://doi.org/10.1039/d5ra00812c

energies than graphite.[14–17] This allows them to be exfoliated down to atomic thickness. Recently, these materials have attracted renewed attention due to their unique structural and electronic properties. Notably, chemically exfoliated monolayer $FePS_3$ has demonstrated efficient photocatalytic hydrogen evolution.[18] Inspired by these findings, monolayers such as $AsGeC_3$, $SbSnC_3$, and $BiPbC_3$ have been investigated, revealing strong stability and excellent optical properties.[19] Additionally, $CoGeSe_3$, $GaSnS_3$, and $InSnS_3$ monolayers show promise as visible-light photocatalysts with high carrier mobility.[20,21] The $GaGeSe_3$ monolayer, in particular, exhibits a solar-to-hydrogen conversion efficiency of 11.33% and a charge carrier mobility of 790.65 $cm^2\ V^{-1}\ s^{-1}$.[22] Substitution is an effective strategy for tuning the electronic properties of monolayers, as demonstrated experimentally. For instance, the MoSSe monolayer was synthesized by replacing the top-layer S atoms with Se atoms.[23] Building on this concept, many quaternary monolayers have been theoretically designed based on the aforementioned ternary structures. The $Zn_2P_2S_3Se_3$ and $Cd_2P_2S_3Se_3$ monolayers are predicted to exhibit exceptionally high charge carrier mobility of 2772 $cm^2\ V^{-1}\ s^{-1}$.[24] Meanwhile, Janus-type monolayers such as $In_2Ge_2Te_3Se_3$, $In_2Ge_2Se_6$, and $In_2Ge_2S_3Se_3$ have emerged as promising candidates for thermoelectric applications in high-temperature environments. In this study, the $Ga_2Ge_2S_3Se_3$ and $Ga_2Ge_2Se_3Te_3$ monolayers were constructed based on the atomic structures of $GaGeS_3$ and $GaGeSe_3$ monolayers, respectively. The structural, electronic and transport properties of the two new monolayers are studied using first-principles calculation.

2 Methodology

All calculations were performed using the Quantum-ESPRESSO package.[25] The Perdew–Burke–Ernzerhof (PBE) functional[26] within the generalized gradient approximation (GGA) and the hybrid functional HSE06 (ref. 27) were employed to describe exchange–correlation effects. Projector augmented-wave (PAW) pseudopotentials[28] were used to represent core-valence electron interactions. An energy cutoff of 520 eV was chosen for effective convergence of the total energies. In addition, a density cutoff, four times the energy cutoff, was used in the calculations. The geometry was fully relaxed until the forces on all of the atoms decreased to less than 0.01 eV $Å^{-1}$ and the total energy change was smaller than 10^{-6} eV. A 15 × 15 × 1 Monkhorst–Pack *k*-point mesh was used to sample the Brillouin zone. The initial structural models of $Ga_2Ge_2S_3Se_3$ and $Ga_2Ge_2Se_3Te_3$ monolayers were constructed based on the known structures of $GaGeS_3$ and $GaGeSe_3$, respectively. The 20 Å vacuum layers were added to avoid interactions between periodic images. The structural asymmetry of $Ga_2Ge_2X_3Y_3$ monolayers induces significant dipole moments, leading to notable van der Waals (vdW) interactions. To accurately account for these vdW interactions, DFT-D3 corrections[29] were incorporated into the DFT functionals. The dynamic stability of the monolayers was assessed by calculating phonon dispersion curves using the functional perturbation method implemented in the PHONOPY code.[30] Transport properties, including carrier mobility, were estimated using the deformation potential method.[31]

3 Results and discussion

3.1 Structural characteristics

The equilibrium configurations of $Ga_2Ge_2X_3Y_3$, shown in Fig. 1, were achieved by optimizing their lattice structures for the lowest energy. The top view of $Ga_2Ge_2X_3Y_3$, as shown in Fig. 1(a), has a hexagonal pattern constructed based on the rhombus unit-cell, which contains 10 constituent atoms including two Ga (green balls), two Ge (purple balls), three S/Se (red balls), and three Se/Te (brown) atoms. As illustrated in Fig. 1(b), these atoms are arranged in five sublayers of S/Se, Ge, Ga, Ge, and Se/Te atoms that are stacked on top of one another. On the right-hand side, Fig. 1(c) shows the dynamic characteristics of these structures in form of phonon dispersions. While $Ga_2Ge_2S_3Se_3$ and $Ga_2Ge_2Se_3Te_3$ monolayers are dynamically stable with positive phonons, the $Ga_2Ge_2S_3Te_3$ monolayer is predicted to be unstable due to the negative frequencies of some acoustic phonons.

It is worth noting that the $Ga_2Ge_2S_3Se_3$ and $Ga_2Ge_2Se_3Te_3$ monolayers are formed by modifying the atomic structures of $GaGeS_3$ and $GaGeSe_3$ monolayers,[22] respectively, where heavier atoms Se/Te are substituted for lighter host atoms S/Se. Such substitutions cause lattice enlargement, as shown in Table 1, the lattice constants ($a = b$) of $Ga_2Ge_2S_3Se_3$ and $Ga_2Ge_2Se_3Te_3$ monolayers are 6.29 Å and 6.74 Å, respectively. These lattice constants are about 0.17–0.28 Å longer than the corresponding values of $GaGeS_3$ or $GaGeSe_3$ monolayer.[22] Due to the stacking of sublayer of identical elements, the substitution of Se atoms for S atoms replaces the whole S-sublayer in the $GaGeS_3$ monolayer[22] (S–Ge–Ga–Ge–S) with the Se-sublayer in the $Ga_2Ge_2S_3Se_3$ monolayer (S–Ge–Ga–Ge–Se). Such a significant change causes noticeable enlargement of all bond-lengths as $GaGeS_3$ monolayer[22] transforms into $Ga_2Ge_2S_3Se_3$ monolayer. As shown in Table 1, the Ge–S, Ga–S, and Ge–Ge bond lengths increase by 0.3–0.13 Å. Consequently, the monolayer thickness, which is defined as the distance between the two edge sublayers, also increases by about 0.08 Å. Similarly, the data listed in Table 1 shows that the replacement of Se-sublayer in $GaGeSe_3$ monolayer[22] with the Te-sublayer in $Ga_2Ge_2Se_3Te_3$ monolayer results in some increase in the Ge–Se, Ga–Se, and Ge–Ge bond lengths by about 0.04–0.22 Å. Meanwhile, the thickness of $Ga_2Ge_2Se_3Te_3$ monolayer is 0.12 eV.

The significant change in the structural characteristics of the two new monolayers requires further study on their stability. From an energy perspective, a new system is considered stable if its total energy is less than the combined energies of its individual components. Such energetic difference is called cohesive energy E_{coh}, which can be calculated for the $Ga_2Ge_2X_3Y_3$ monolayers as follows:

$$E_{coh} = \frac{2E_{Ga} + 2E_{Ge} + 3E_X + 3E_Y - E_{tot}}{10}, \quad (1)$$

where, E_{tot} represents the total energy of the $Ga_2Ge_2S_3Se_3$ and $Ga_2Ge_2Se_3Te_3$ monolayers. E_{Ga}, E_{Ge}, E_X, E_Y represents the total energy of isolated Ga, Ge, S, or Se atom. The cohesive energies of $Ga_2Ge_2S_3Se_3$ and $Ga_2Ge_2Se_3Te_3$ monolayers are 4.20 eV and 3.78 eV, respectively. These values indicate that the formations of the two monolayers are energetically favorable. Such cohesive

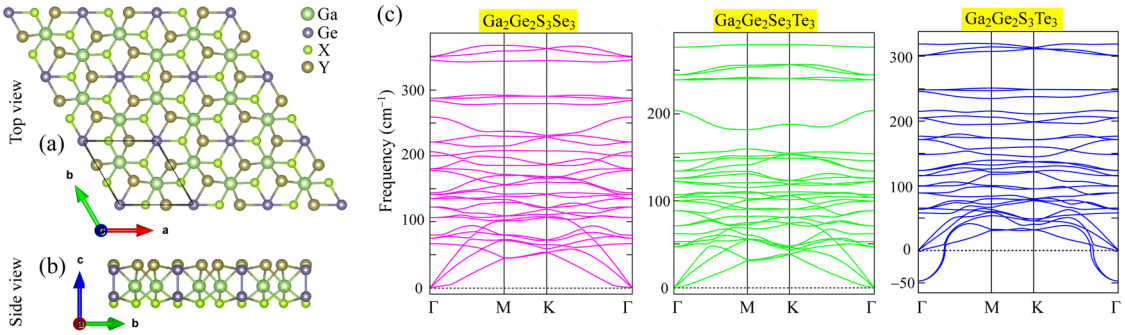

Fig. 1 Optimized atomic structure of $Ga_2Ge_2X_3Y_3$ (X/Y = S, Se, Te; X ≠ Y) monolayers shown in (a) top view and (b) site view together with (c) their phonon dispersions.

Table 1 Lattice constant *a*, thickness *h*, and interatomic distance *d*, cohesive energy E_{coh}, PBE/HSE06 bandgap E_g, elastic coefficient C_{ij}, Young's modulus Y_{2D} and Poisson's ratio ν_{2D} of $Ga_2Ge_2S_3Se_3$, $Ga_2Ge_2Se_3Te_3$ monolayers

	a (Å)	*h* (Å)	d_{Ge-X} (Å)	d_{Ga-X} (Å)	d_{Ge-Ge} (Å)	d_{Ge-Y} (Å)	d_{Ga-Y} (Å)	E_{coh} (eV per atom)	E_g^{PBE} (eV)	E_g^{HSE06} (eV)	C_{11} (N m^{-1})	C_{12} (N m^{-1})	C_{66} (N m^{-1})	Y_{2D} (N m^{-1})	ν_{2D}
$Ga_2Ge_2S_3Se_3$	6.29	3.28	2.37	2.66	2.37			4.20	1.02	1.83	76.69	29.55	23.57	65.31	0.39
$Ga_2Ge_2Se_3Te_3$	6.74	3.50			2.42	2.57	2.87	3.78	0.06	0.63	59.82	24.21	17.81	50.02	0.41

energies can also be regarded to be typical values for the $A_2B_2X_3Y_3$ family, as other members, namely $Al_2Ge_2S_3Se_3$ and $Al_2Ge_2Se_3Te_3$ monolayers, have similar cohesive energies (4.10–4.59 eV).[32] The thermal stabilities of the two monolayers are evaluated by analyzing the changes in their total energies at 300 K (room temperature) and at 500 K during an *ab initio* molecular dynamics (AIMD) simulation. As shown in Fig. 2(a) and (b), respectively, the total energies of $Ga_2Ge_2S_3Se_3$ and $Ga_2Ge_2Se_3Te_3$ monolayers vary within a very small deviation ranging from 0.8 to 1.0 eV. This slight energy fluctuation quickly decreases after the first 1–2 picoseconds. This result rules out the possibility of heat-induced structural damage, confirming that $Ga_2Ge_2S_3Se_3$ and $Ga_2Ge_2Se_3Te_3$ monolayers are stable at room temperature and at higher temperature of 500 K.

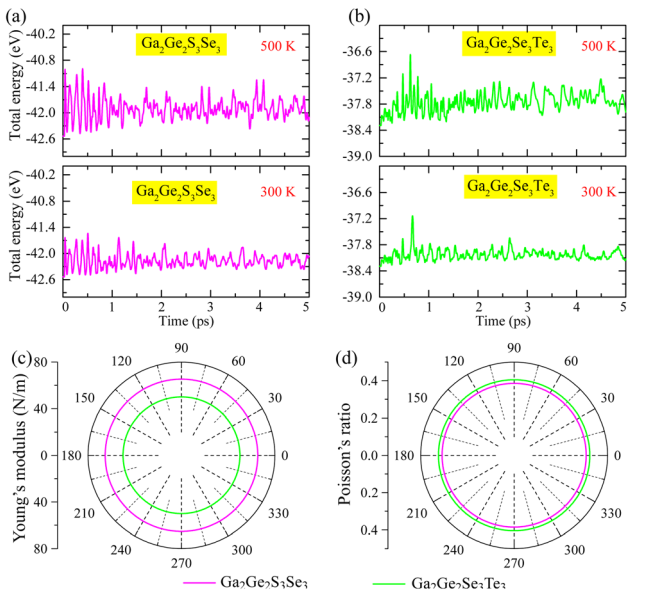

Fig. 2 (a and b) Total energy variation of $Ga_2Ge_2S_3Se_3$ and $Ga_2Ge_2Se_3Te_3$ monolayers at 300 K and 500 K; angular functions of (c) Young's modulus and (d) Poisson's ratio of $Ga_2Ge_2S_3Se_3$ (pink circles) and $Ga_2Ge_2Se_3Te_3$ (green circles) monolayers.

The mechanical stability, stiffness and deformation behavior of 2D materials, such as graphene, transition metal dichalcogenides, and MXenes, *etc.*,[33–35] can be analyzed using Born's stability criteria, Young's modulus (Y) and Poisson's ratio (ν), respectively. These properties are determined from the elastic constants C_{11}, C_{12}, and C_{66}, which are derived by calculating the second partial derivatives of the total energy of the system with respect to the corresponding components of strain, thereby linking the material's atomic-level interactions to its macroscopic mechanical properties.[36]

For 2D hexagonal materials such $Ga_2Ge_2S_3Se_3$ and $Ga_2Ge_2Se_3Te_3$ monolayers, the Born's mechanical stability criteria are simplified due to their symmetry and two-dimensional nature as follows: $C_{11} > 0$, $C_{66} > 0$, and $C_{11} - C_{12} > 0$.[37,38] As reported in Table 1, the calculated C_{11}, C_{12} and C_{66} moduli of $Ga_2Ge_2S_3Se_3$ and $Ga_2Ge_2Se_3Te_3$ monolayers comply these criteria. These findings are crucial, as the Born criteria ensure the strength of materials under small deformations and indicate the absence of lattice instabilities. Furthermore, the Young's modulus and Poisson's ratio as angular functions were calculated in the *xy* plane. As plotted in Fig. 2(c) and (d) for $Ga_2Ge_2S_3Se_3$ and $Ga_2Ge_2Se_3Te_3$ monolayers, respectively, the graphs of these functions are nearly perfect circles. This angular dependence directly correlates with the structural isotropy and uniformity of these monolayers, underscoring their potential for applications where uniform mechanical properties are essential.[39,40] The calculated Young's

modulus values are 65.31 N m^{-1} for $Ga_2Ge_2S_3Se_3$ and 50.02 N m^{-1} for $Ga_2Ge_2Se_3Te_3$, placing them among 2D materials with moderate stiffness such as $GaGeSe_3$, $GaGeS_3$, $Al_2Ge_2S_3Se_3$, $Al_2Ge_2Se_3Te_3$, tinselenidene and bismuth telluride nanosheets.[22,32,41,42] Meanwhile, $Ga_2Ge_2S_3Se_3$ and $Ga_2Ge_2Se_3Te_3$ monolayers are more flexible than phosphorene, graphene, black phosphorus (BP), hexagonal boron nitride and MoS_2 monolayer.[43–45] The reduced modulus compared to graphene can be attributed to the buckled structure and the chemical composition of these monolayers, which result in lower in-plane bonding strength. This intermediate stiffness makes $Ga_2Ge_2S_3Se_3$ and $Ga_2Ge_2Se_3Te_3$ suitable for applications requiring flexibility without significant loss of mechanical stability. In addition, the Poisson's ratios of $Ga_2Ge_2S_3Se_3$ and $Ga_2Ge_2Se_3Te_3$ range from 0.39 to 0.41, exceeding those observed in many ternary and quaternary monolayers of similar atomic structures, including $GaGeS_3$, $GaGeSe_3$, and $Al_2Ge_2Se_3Te_3$.[22,32] A high Poisson's ratio indicates the material's ability to undergo lateral expansion when stretched, which is a desirable trait for enhancing toughness and ductility. For comparison, the Poisson's ratios of typical 2D transition metal dichalcogenides MoS_2 and WS_2, tin chalcogenides, boron nitride (h-BN)[46–48] hover around 0.3, making $Ga_2Ge_2S_3Se_3$ and $Ga_2Ge_2Se_3Te_3$ superior in terms of toughness and deformation resilience.

This combination of moderate stiffness and high Poisson's ratio suggests that $Ga_2Ge_2S_3Se_3$ and $Ga_2Ge_2Se_3Te_3$ monolayers can endure significant deformation without losing their structural integrity. The demonstration of FeClF, MnSeTe, and MnSTe monolayers as promising materials for a wide range of electronic applications, particularly due to their favorable elastic properties,[49,50] provides strong support for considering $Ga_2Ge_2S_3Se_3$ and $Ga_2Ge_2Se_3Te_3$ as potential candidates for flexible electronic devices, such as foldable displays, wearable sensors, and stretchable photovoltaics, where both mechanical resilience and flexibility are required.[51–53] Furthermore, their structural and mechanical characteristics could enable their integration into composite materials to enhance performance under mechanical stress.

3.2 Electronic characteristics of $Ga_2Ge_2S_3Se_3$ and $Ga_2Ge_2Se_3Te_3$ monolayers

Fig. 3 presents the band structures of $Ga_2Ge_2S_3Se_3$ and $Ga_2Ge_2Se_3Te_3$ monolayers, calculated using both HSE06 (solid pink curves) and GGA-PBE (dashed blue curves) functionals. Both monolayers exhibit analogous band structure patterns, characterized by a high density of electronic states due to the large number of atoms in their unit cells. Notably, both materials possess direct band gaps, with the valence band maximum

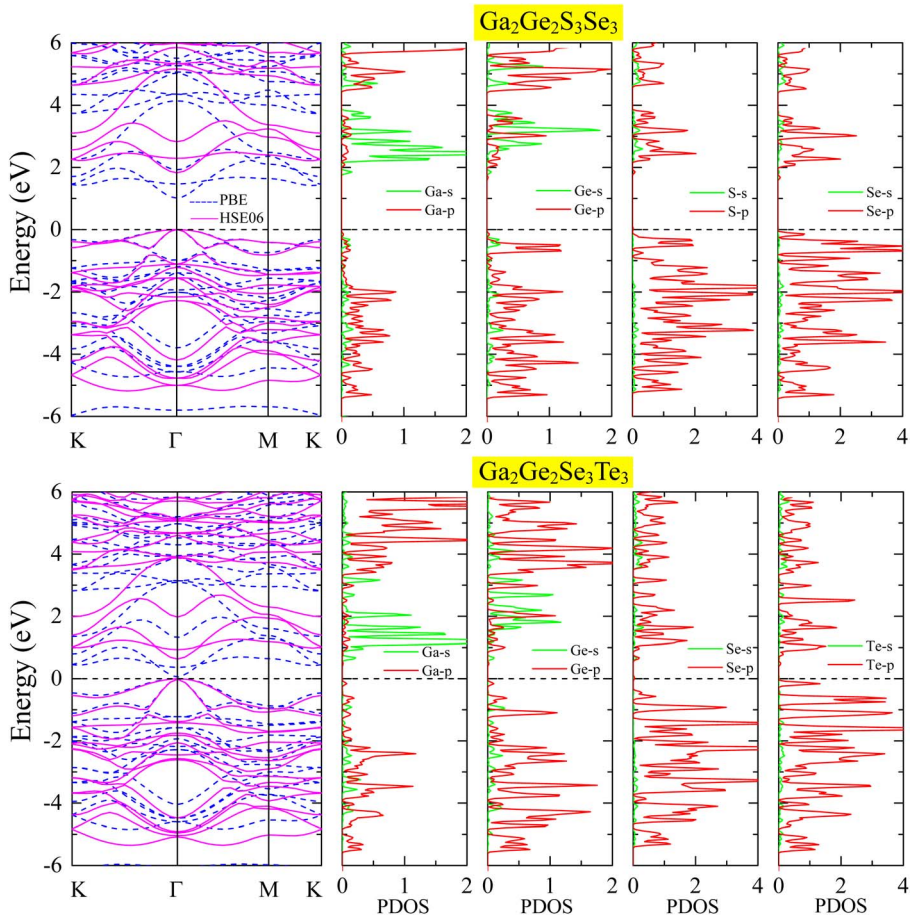

Fig. 3 Electronic band structures and projected density of states (PDOS) of$Ga_2Ge_2S_3Se_3$ and $Ga_2Ge_2Se_3Te_3$ monolayers. The band structures were calculated using PBE functional (dash blue lines) and HSE06 hybrid functional (solid pink lines).

(VBM) and conduction band minimum (CBM) situated at the Γ – point. The HSE06 method offers a more accurate treatment of the exchange–correlation interaction, effectively suppressing the unphysical overestimation of electron energies in the valence bands. As a result, the calculated band gap between the valence and conduction bands is significantly larger in the HSE06 approach compared to the values calculated by the GGA-PBE method. For the $Ga_2Ge_2S_3Se_3$ monolayer, the HSE06 calculation yields a band gap of 1.83 eV, which is 0.81 eV larger than the value calculated by the GGA-PBE method. In the case of the $Ga_2Ge_2Se_3Te_3$ monolayer, the GGA-PBE method predicts an extremely narrow band gap of 0.06 eV. However, the HSE06 approach provides a significantly improved result, revealing a band gap of 0.63 eV.

Compared to the HSE06 band gaps of $GaGeS_3$ (2.51 eV) and $GaGeSe_3$ (1.91 eV) monolayers,[22] replacing the S sublayer with a Se sublayer or the Se sublayer with a Te sublayer reduces the band gaps of the original monolayers. These results highlight that substituting heavier element provides an efficient strategy for narrowing the band gaps of monolayers. This effect results from the increased spin–orbit coupling (SOC) induced by heavier atoms, which brings the conduction and valence band edges closer together.[54,55] In two-dimensional materials, the impact of SOC is further amplified by quantum confinement,[56,57] leading to more pronounced band gap reductions and tunable electronic properties. The band gap of $Ga_2Ge_2Se_3Te_3$ is below 1.23 eV, rendering it unsuitable as a photocatalyst for water splitting due to insufficient energy for driving the reaction.[58] In contrast, the $Ga_2Ge_2S_3Se_3$ monolayer is well-suited for this application. Additionally, it represents an advancement over the $GaGeS_3$ monolayer,[22] as its narrower band gap enables greater absorption of visible light, which makes up a significant portion of the solar energy spectrum. In the $Ga_2Ge_2S_3Se_3$ monolayer, the PDOS reveals that p-orbitals from Ga, Ge, S, and Se dominate both the valence and conduction bands across a wide energy range. Strong hybridization is observed, particularly between the s- and p-orbitals of Ga and Ge. The direct bandgap is formed by the valence band maximum (VBM) dominated by Se-p orbitals and the conduction band minimum (CBM) dominated by Ga-s orbitals. A similar PDOS profile is observed in the $Ga_2Ge_2Se_3Te_3$ monolayer, with p-orbitals from the constituent atoms dominating at all energy levels. The VBM is primarily composed of Te-p orbitals, while the CBM is dominated by Se-s, p orbitals and p-orbitals from the other atoms.

To gain deeper insights into the orbital contributions of each constituent element to the electronic band structure, we analyzed the projected band structures of $Ga_2Ge_2S_3Se_3$ and $Ga_2Ge_2Se_3Te_3$ monolayers, as depicted in Fig. 4. In these plots, the s, p_x, p_y, and p_z orbitals are depicted in blue, pink, red, and green, and their relative contributions are visualized by the size of the corresponding spheres. By examining these projected band structures, we can identify the specific orbitals of each element that dominate the formation of the valence band

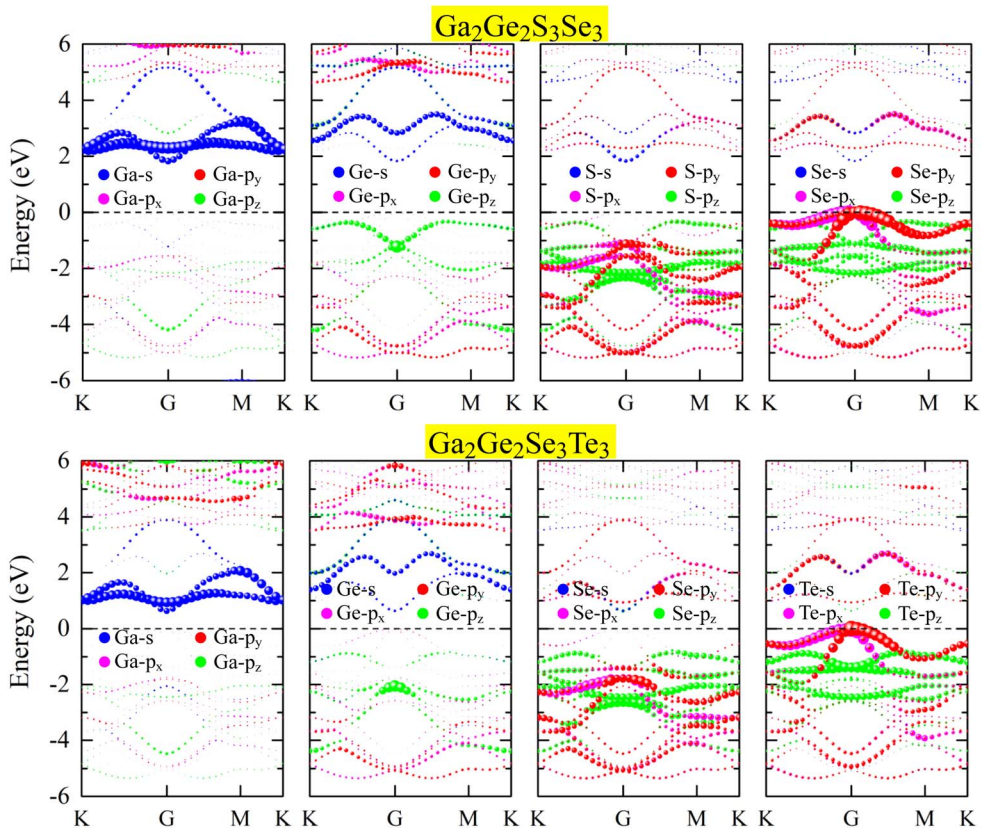

Fig. 4 Orbital-projected band structures of $Ga_2Ge_2S_3Se_3$ and $Ga_2Ge_2Se_3Te_3$ monolayers.

maximum and conduction band minimum, providing valuable information about the electronic and hole transport properties of these materials. It is obvious that the highest valence bands are mainly occupied by Se-p orbitals in $Ga_2Ge_2S_3Se_3$ monolayer and by Te-p orbitals in $Ga_2Ge_2Se_3Te_3$ monolayer. Consequently, the width of the band gap is partially determined by the substituted Se or Te element. It is worth noting that the lowest conduction bands, on the other hand, are mainly constructed by the Ga-s orbitals, making them another important factor in creating the band gap.

In $Al_2Ge_2S_3Se_3$ and $Al_2Ge_2Se_3Te_3$ monolayers, the bandgaps range from 1.07 to 2.38 eV.[32] These values are smaller than those observed in $Ga_2Ge_2S_3Se_3$ and $Ga_2Ge_2Se_3Te_3$ monolayers. This reduction in bandgap can be attributed to the lighter atomic mass of Al compared to Ga, resulting in weaker SOC effects in the Al-containing compounds. When analyzing the bandgaps of $In_2Ge_2S_3Se_3$, $In_2Ge_2S_3Te_3$, $Al_2Ge_2S_3Se_3$, and $Al_2Ge_2Se_3Te_3$ monolayers[32,59] within the $A_2B_2X_3Y_3$ family, it is observed that the Y atoms (Se or Te) play a significant role in determining the bandgap width. Specifically, heavier Y atoms result in narrower bandgaps. These findings confirm the mechanism discussed in the previous section, which emphasizes the significant influence of SOC on bandgap values. At lower valence bands, ranging from −2 to −1 eV, orbital hybridization is observed to happen between p_z orbitals from Ge, S, and Se elements in $Ga_2Ge_2S_3Se_3$ monolayer or Ge, Se, and Te elements in $Ga_2Ge_2Se_3Te_3$ monolayer. The hybridization of other orbitals happens in the deeper energy levels. Meanwhile, the p_y orbitals from Se or Te atoms participate in the hybridization with other orbitals at almost all valence energy bands, showing the important role of Se and Te elements in the formation of covalent bonds in $Al_2Ge_2S_3Se_3$ and $Al_2Ge_2Se_3Te_3$ monolayers.

3.3 Photocatalytic performance of $Ga_2Ge_2S_3Se_3$ monolayer

Fig. 5(a) illustrates the variation in electrostatic potential across both sides of the $Ga_2Ge_2S_3Se_3$ monolayer. To move an elementary charge away from the monolayer's surface, work must be done against the electrostatic potential. The horizontal blue line in the diagram represents the vacuum level, where a free electron is no longer influenced by the material's potential. The work function (Φ) is defined as the energy required to move an electron from the Fermi level to the vacuum level. Due to the higher electronegativity of S compared to Se, the S-side of the monolayer exhibits a higher electrostatic potential. This results in a difference in work function ($\Delta\Phi$) of 0.27 eV between the two sides of the monolayer. As a result, an internal electric field E is induced,[60] pointing from the lower-potential Se-side to the higher-potential S-side. This field facilitates the movement of photoexcited electrons from the S-side to the Se-side, while photoexcited holes move in the opposite direction. This promotes effective electron–hole separation, which not only enhances the material's photocatalytic efficiency but also influences the band edge alignment relative to the redox potential.[60] The energies of the conduction band edge E_{CBE} and valence band edge E_{VBE} can be defined by formula proposed by Toroker *et al.*[61,62] based on the energy at vacuum level E_V and the energies of the unshifted conduction band minimum E_{CBM} and valence band maximum E_{VBM} as $E_{CBE/VBE} = E_{CBM} - E_V^{S/Se\text{-}side}$. In Fig. 5(a), the positions of E_{VBE} and E_{CBE} are denoted with green and red solid rectangles, respectively. It is obvious that the E_{VBE} is located below the oxidation potential O_2/H_2O and the E_{CBE} is above the H^+/H_2 reduction potential. Therefore, it is expected that the $Ga_2Ge_2S_3Se_3$ monolayer can induce the separation of water to release oxygen and hydrogen gases if the energetic requirements are met. In Fig. 5(a), the positions of E_{VBE} and E_{CBE} are denoted by green and red solid rectangles, respectively. The diagram shows that the E_{VBE} is positioned below the oxidation potential of water (O_2/H_2O), while the E_{CBE} lies above the reduction potential of protons (H^+/H_2). This band alignment is typical for water splitting photocatalyst.

Strain engineering emerges as a powerful tool for enhancing the photocatalytic activity of two-dimensional materials, particularly Janus structures like $Ga_2Ge_2S_3Se_3$. By applying strain, precise control over the bandgap and band alignment becomes possible. This allows for optimization of light

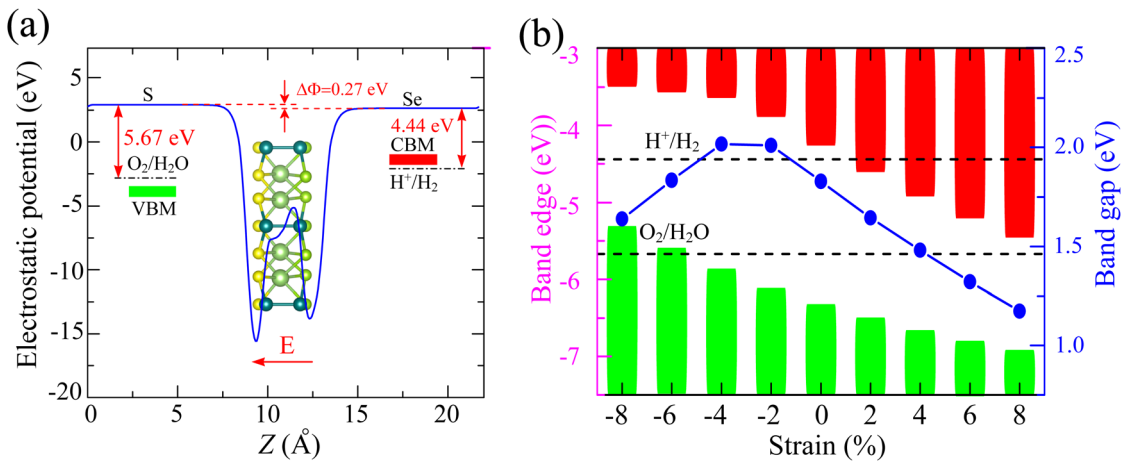

Fig. 5 (a) Electrostatic potential with intrinsic electric field (red arrow) of $Ga_2Ge_2S_3Se_3$ monolayer and (b) the variation of bandgap and band edge alignment relative to the redox potential of water splitting reaction.

absorption and efficient charge carrier transport, crucial for driving photocatalytic reactions.[63–66] Furthermore, strain can effectively align the band edges with the redox potentials of water splitting reactions. This alignment facilitates efficient charge transfer and improves the overall catalytic efficiency.[67,68] Most of 2D materials can withstand substantial strains, typically up to around 10%,[69] before significant deformation or failure. This high flexibility stems from their unique atomic structure. However, it's crucial to recognize that this value is not universal and depends strongly on the specific material and the nature of the applied strain. For example, reported strain limits for 2D GeP range from 12.9% to 26.2%,[70] and MoS_2 monolayers have been shown to maintain stability above 10% strain.[71] The $Ga_2Ge_2S_3Se_3$ and $Ga_2Ge_2Se_3Te_3$ monolayers, with their moderate Young's moduli (50.02–65.31 N m^{-1}) and high Poisson's ratios (0.39–0.41), are predicted to be relatively flexible. Therefore, the compressive and tensile strains ranging from −8% to 8% were applied on these two monolayers. Our investigation delves into the impact of strain on the bandgap and band edge alignment of the $Ga_2Ge_2S_3Se_3$ monolayer (Fig. 5(b)). Compressive strains ranging from −2% to −4% lead to a bandgap widening of approximately 2.0 eV. Beyond this range, both further compression and tensile strains result in a bandgap reduction. Notably, the band edges of the $Ga_2Ge_2S_3Se_3$ monolayer remain suitable for water redox reactions when subjected to compressive strains between −6% and −8% or tensile strains below 4%.

Strain engineering offers a versatile approach to fine-tune the electronic and optical properties of 2D materials, including their bandgap, band edge positions, and light absorption characteristics. These tunable properties hold significant potential for enhancing photocatalytic performance in applications such as water splitting.[72–74] Given the promising photocatalytic potential of $Ga_2Ge_2S_3Se_3$ monolayer, we investigated the effects of strain ranging from −8% to 8%. The resulting changes in band structure and light absorption rate are illustrated in Fig. 6, respectively.

Fig. 6(a) presents the band structures with the valence band maximum (VBM) aligned to the Fermi level, allowing us to focus on the shifts in the conduction band minimum (CBM). Previous studies on black phosphorus, transition metal dichalcogenides, and ternary Janus monolayers have demonstrated that strain can induce significant band structure modifications, such as direct-to-indirect bandgap transitions, bandgap tuning, and changes in band curvature.[75,76] In contrast, the $Ga_2Ge_2S_3Se_3$ monolayer maintains a direct bandgap configuration under both compressive and tensile strain, with the VBM and CBM remaining at the Γ – point. Notably, the curvature of the conduction bands increases significantly under strain compared to the unstrained monolayer (Fig. 3). This increased curvature suggests a reduced effective mass of electrons, potentially leading to enhanced electron mobility.

The variation in electronic structure, particularly the changes in bandgap discussed above, significantly influences the optical properties of $Ga_2Ge_2S_3Se_3$ monolayers. Fig. 6(b) presents the calculated absorption rates, $\alpha(\omega)$, for the monolayer under strains ranging from −8% to 8%. The unstrained $Ga_2Ge_2S_3Se_3$ monolayer exhibits a relatively high absorption rate (black curve), exceeding 10^5 cm^{-1} in the infrared region and increasing further in the visible region. In the ultraviolet region, the absorption rate surpasses 10^6 cm^{-1}. This strong absorption across a broad spectral range, including the infrared and visible regions, makes $Ga_2Ge_2S_3Se_3$ a promising candidate for solar energy applications, as these regions contain the majority of solar energy reaching Earth. Compressive strains (−4% and −8%) lead to a widening of the bandgap, resulting in a reduced absorption of infrared and visible light. However, these larger bandgaps enable the absorption of higher-energy ultraviolet photons. Conversely, tensile strains (4% and 8%) narrow the bandgap, enhancing the absorption of infrared and visible light.

A critical step in water splitting involves the adsorption of hydrogen atoms onto the catalyst surface, facilitating electron transfer. This adsorption process induces a change in the system's total energy, which can be analyzed through Gibbs free energy calculations. To calculate the change in Gibbs free energy for the $Ga_2Ge_2S_3Se_3$ monolayer, it is necessary to

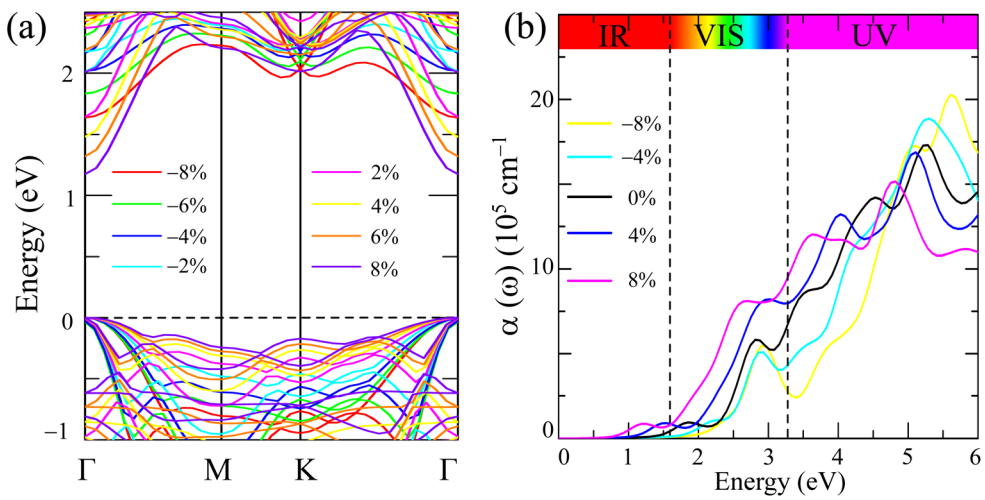

Fig. 6 (a) Impact of strain on the band structure and (b) the light absorption rate of the $Ga_2Ge_2S_3Se_3$ monolayer.

determine the total energies of hydrogen-adsorbed system $E_{Ga_2Ge_2S_3Se_3+H}$, pristine $Ga_2Ge_2S_3Se_3$ monolayer $E_{Ga_2Ge_2S_3Se_3}$, and isolated hydrogen molecule E_{H_2}. Then the change in energy ΔE_H is calculated as $\Delta E_H = E_{Ga_2Ge_2S_3Se_3+H} - E_{Ga_2Ge_2S_3Se_3} - 0.5E_{H_2}$, and the Gibbs free energy ΔG_H is defined as $\Delta G_H = \Delta E_H + 0.24$ eV.[77–79] Fig. 7(a) and (b) depicts the Gibbs free energy diagram of the $Ga_2Ge_2S_3Se_3$ monolayer, wherein the bottom and top surfaces are designated as the S-side and Se-side, respectively. The calculated ΔG_H values at the Ga, Ge, and Se sites exhibit negative values, ranging from −0.95 to −2.01 eV. The negative ΔG_H suggests that the adsorption of hydrogen atoms at these specific sites is thermodynamically favorable.

The $Ga_2Ge_2S_3Se_3$ monolayer's capacity for photocatalytic water splitting can be assessed by examining the thermodynamic feasibility of both the Hydrogen Evolution Reaction (HER) and the Oxygen Evolution Reaction (OER).[59,80] The Gibbs free energy changes (ΔG) associated with each of these half-reactions at pH = 0 are shown in Fig. 7(c) and (d). The OER half-reaction on the $Ga_2Ge_2S_3Se_3$ monolayer involves a series of steps. Initially, energy is required to break the O–H bond in water to form an adsorbed hydroxyl ion (OH*). Subsequently, this hydroxyl ion undergoes further oxidation to generate an adsorbed oxygen atom (O*). The adsorbed oxygen atom then reacts with another water molecule to form a hydroperoxide intermediate (OOH*), which finally decomposes to release molecular oxygen (O_2). In the absence of light irradiation (U = 0 eV), the calculated ΔG values for these four steps are 1.38 eV, 3.71 eV, 4.64 eV, and 4.92 eV, respectively. The highest energy barrier, and thus the potential-determining step, is the transformation from OOH* to O_2. As mentioned in previous sections, the electronic characteristics of $Ga_2Ge_2S_3Se_3$ monolayer is favorable for the generation of photoexcited electron–hole pairs. The photogenerated holes in the valence bands can effectively interact with the intermediate species formed during the OER half-reactions, thereby facilitating the subsequent oxidation steps. Upon illumination, the energy barriers for the OER steps are modified. The calculation method of energy barriers of the illuminated material is presented in ESI.† As shown in Fig. 7(d), these effective barriers are reduced to negative or near-zero values, indicating that the OER steps become spontaneous or require minimal activation energy. These results strongly suggest that light irradiation can effectively trigger the OER half reactions on the $Ga_2Ge_2S_3Se_3$ monolayer spontaneously.

In water splitting, the OER oxidizes water to produce oxygen O_2, protons H^+, and electrons. These products are subsequently utilized by the HER to generate hydrogen gas H_2. However, the thermodynamic feasibility of this process is governed by the change in Gibbs free energy ΔG. Fig. 7(c) illustrates the ΔG for the HER process on the $Ga_2Ge_2S_3Se_3$ monolayer. Without light irradiation, the formation of adsorbed hydrogen atoms H* requires an energy input of 1.36 eV. Under light irradiation,

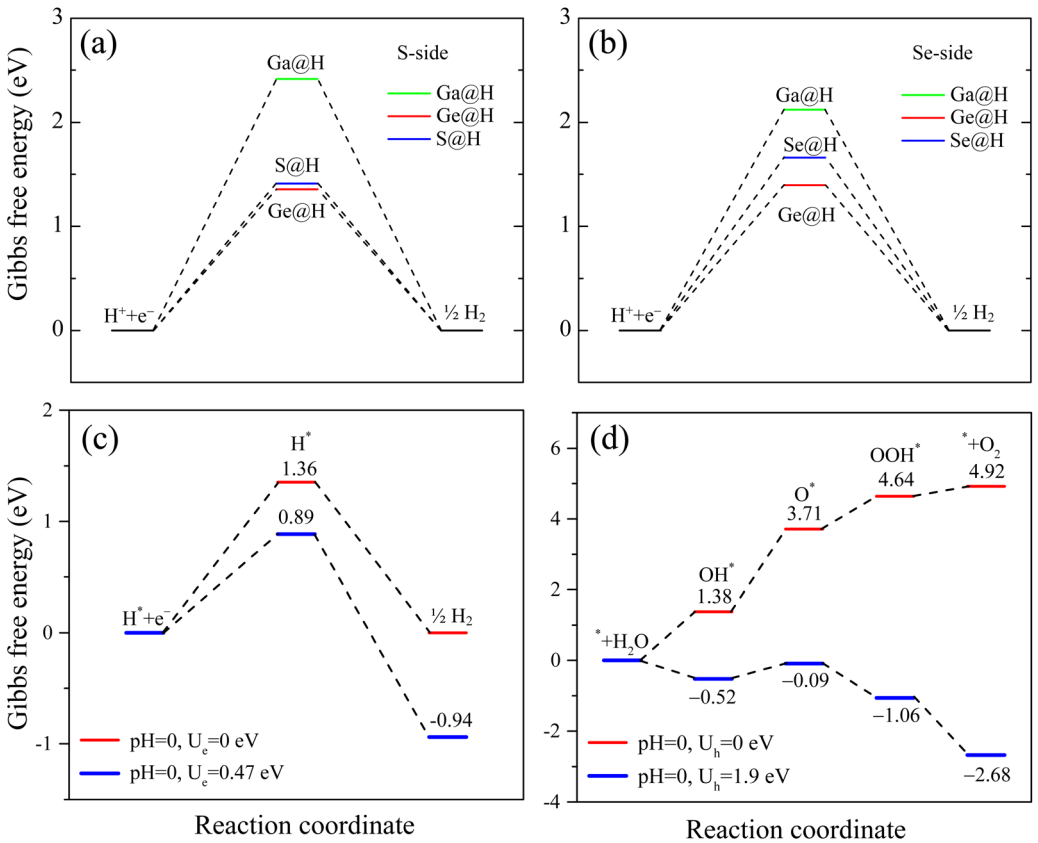

Fig. 7 (a and b) Gibbs free energy change as hydrogen atom is connected to the Ga, Se, or Ge atoms on the S-side and Se-side of in $Ga_2Ge_2S_3Se_3$ monolayer; (c and d) photocatalytic reaction steps of HER and OER half-reactions.

photogenerated electrons contribute an external potential of U = 0.47 eV, effectively reducing the HER reaction barrier on the Janus $Ga_2Ge_2S_3Se_3$ to 0.89 eV. Many promising photocatalysts exhibit positive HER reaction barriers, which can be mitigated through various strategies such as adsorbing alkali and transition metals,[81] constructing heterojunctions,[82] and introducing point defects like vacancies.[83] In practice, applying an external bias voltage can significantly enhance the separation of photogenerated electron–hole pairs, thereby improving the overall photocatalytic efficiency. For example, studies have demonstrated that combining a TiO_2 photoanode with an organophotocathode enables stoichiometric water decomposition at bias voltages below the theoretical minimum of 1.23 V. This exemplifies the effectiveness of external voltage in lowering the energy barrier for water splitting reactions and boosting photocatalytic activity. However, the wide bandgap of TiO_2 (approximately 3.2 eV) restricts its activity to the ultraviolet region of the solar spectrum, which constitutes a relatively small portion of solar energy.[84] Therefore, the $Ga_2Ge_2S_3Se_3$ monolayer, with its moderate bandgap and low HER energy barrier, emerges as a promising candidate for efficient hydrogen generation through photocatalytic water splitting.

To calculate the charge carrier mobility, it is necessary to establish the dependence of the system total energy E_{total} and band edges E_{edge} (the positions of VBM and CBM) as functions of the uniaxial strains ε_{uni}. As shown in Fig. 8(a), the E_{total} values are calculated at 5 discrete values of the ε_{uni}, which ranges from −1% to 1%. The E_{edge} values, as shown in Fig. 8(b), are also determined at these discrete values of uniaxial strains. Therefore, an interpolation model was applied to construct the continuous functions E_{total} and E_{edge}, making it possible to the determine the elastic modulus C_{2D} by taking the second derivative of the total energy function and divided by the area of the unit-cell. Meanwhile, the deformation energy E_{def} is derived from the Laplacian of E_{edge} the edge energy function. The charge carrier mobility in 2D material, μ_{2D}, is then defined as $\mu_{2D} = e\hbar^3 C_{2D}/k_B T m^* \bar{m}^* {E_{def}}^2$, where e, $\hbar$, k_B, and T represent charge of a free electron, the temperature in kelvin, the reduced Planck constant, and the Boltzman constant, respectively. The symbol $\bar{m}^*$ is the average value of the effective masses m^*, which is defined based on the energy function of k – point $E(k)$ as $m^* = (\hbar^2 \partial^2 E_k/\partial^2 k)^{-1}$.

The $Ga_2Ge_2S_3Se_3$ monolayer exhibits nearly isotropic electron mobility in the range of 430.82–461.50 $cm^2\ V^{-1}\ s^{-1}$, enabling efficient charge transport in all directions. This isotropic mobility minimizes anisotropic losses that can hinder device performance in complex architectures.[85,86] Moreover, the $Ga_2Ge_2S_3Se_3$'s electron mobility is comparable to well-established 2D photocatalysts like MoS_2, PdS_2, $PdSe_2$, SnP_2S_6, and As_2S_3,[87–91] facilitating rapid electron transport to the reduction site for reactions such as hydrogen evolution. The $Ga_2Ge_2S_3Se_3$ monolayer exhibit significantly higher electron mobility compared to their hole mobility (19.55–33.47 $cm^2\ V^{-1}\ s^{-1}$). This disparity can suppress electron–hole recombination, a major loss mechanism in photocatalytic processes.

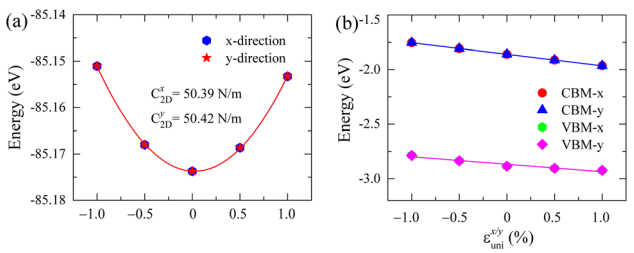

Fig. 8 (a) Total energy E_{total} and (b) band edge energy E_{edge} as functions of uniaxial strains ε_{uni} applied on the $Ga_2Ge_2S_3Se_3$ monolayer.

The previous sections have established $Ga_2Ge_2S_3Se_3$ monolayer as a promising material for photocatalytic applications. Its 1.83 eV bandgap aligns well with the solar spectrum, making it an ideal candidate for sunlight-driven water splitting. To further explore its potential, additional calculations were performed to assess its performance in this process. The solar-to-hydrogen efficiency η_{STH} of $Ga_2Ge_2S_3Se_3$ monolayer, a measure for its ability to convert solar energy into hydrogen, is determined by two primary factors: light absorption efficiency η_{abs} and carrier utilization efficiency η_{cu}. As outlined in equations $\eta_{STH} = \eta_{abs} \times \eta_{cu}$,[92] η_{abs}, which quantifies the photocatalyst's ability to absorb sunlight, is primarily governed by the semiconductor's bandgap E_g. The $Ga_2Ge_2S_3Se_3$ monolayer exhibits a high light absorption rate $\alpha(\omega)$ of 10^5–10^6 cm^{-1} across a broad spectral range from infrared to ultraviolet, leading to the η_{abs} of 32.18%. Carrier utilization efficiency η_{cu}, on the other hand, reflects the efficiency of converting absorbed sunlight into usable charge carriers. As shown in the supplementary, this parameter is influenced the bandgap E_g. The calculated value of η_{cu} is 47.54%. Based on the values of η_{abs} and η_{cu}, the η_{STH} of $Ga_2Ge_2S_3Se_3$ monolayer is predicted to be 15.30%. However, this value must be corrected[92] because in the Janus monolayers with difference in vacuum level (ΔE_V), the intrinsic electric field can do positive work W_{in} in separating the electron–hole pair. As defined in the discussion regarding to Fig. 5(a), the ΔE_V equals to the difference in work function $\Delta\Phi$, which is 0.27 eV. With $P(\hbar\omega)$ is the AM1.5G solar energy flux, the work W_{in} is determined as $W_{in} = \Delta E_V \int_{E_g}^{\infty} \frac{P(\hbar\omega)}{\hbar\omega} d(\hbar\omega)$. Therefore, the total work for photocatalytic process becomes $\int_0^{\infty} P(\hbar\omega)d(\hbar\omega) + W_{in}$. The actual efficiency (η'_{STH}) is $\eta'_{STH} = \eta_{STH} \times \int_0^{\infty} P(\hbar\omega)d(\hbar\omega)/(\int_0^{\infty} P(\hbar\omega)d(\hbar\omega) + W_{in})$. Applying this correction, the efficiency of $Ga_2Ge_2S_3Se_3$ monolayer becomes 14.80%, making this monolayer a promising candidate for photon-driven water splitting photocatalysis. As mentioned above, a water splitting photocatalyst must meet many strict requirements. Therefore, to achieve the η'_{STH} in the range of 3.33–16%, a monolayer is usually modified by elemental substitution, phase transitions, or the application of strain.[22,59,62,93,94] The $Ga_2Ge_2S_3Se_3$ monolayer offers several advantages over its parent $GaGeS_3$ monolayer.[22] Notably, its solar-to-hydrogen conversion efficiency (14.80%) surpasses that of $GaGeS_3$ (11.33%). The transition from an indirect to a direct bandgap in $Ga_2Ge_2S_3Se_3$ enhances light absorption and facilitates faster charge separation. While direct bandgap materials are often susceptible to rapid electron–hole recombination, this effect is mitigated in

$Ga_2Ge_2S_3Se_3$ due to an intrinsic electric field that promotes charge separation. Consequently, the substitution of Se for S results in a monolayer with demonstrably improved photocatalytic properties.

4 Conclusion

This work employed first-principles calculations to explore potential photocatalytic water splitting materials within the $A_2B_2X_3Y_3$ family. Structural investigations revealed that $Ga_2Ge_2Se_3Te_3$ monolayer is unstable, while $Ga_2Ge_2S_3Se_3$ and $Ga_2Ge_2Se_3Te_3$ monolayers exhibit both dynamic and thermal stability. Furthermore, elastic parameter analysis demonstrates a favorable balance between flexibility and stiffness in these monolayers, making them suitable for flexible applications. Electronic structure analysis of $Ga_2Ge_2S_3Se_3$ and $Ga_2Ge_2Se_3Te_3$ monolayers indicates that orbital contributions from Ga and Y atoms within the $Ga_2Ge_2X_3Y_3$ formula play a crucial role in determining the bandgap values. This finding suggests a straightforward approach to tune the bandgap of $Ga_2Ge_2X_3Y_3$ materials, enabling a broader range of applications. While the bandgap of $Ga_2Ge_2Se_3Te_3$ monolayer (0.63 eV) is too narrow for efficient photocatalytic water splitting, the bandgap of $Ga_2Ge_2S_3Se_3$ monolayer (1.83 eV) positions it as a promising candidate. Further investigations reveal several key advantages of $Ga_2Ge_2S_3Se_3$ monolayer for photocatalytic water splitting applications. A significant difference of 0.27 eV in the work functions between the S-side and Se-side of the monolayer induces an intrinsic electric field, effectively driving photoexcited electrons from the Se-side to the S-side and facilitating efficient charge separation. The band edge alignment of $Ga_2Ge_2S_3Se_3$ monolayer is well-suited for triggering the photoexcited redox reactions involved in water splitting. This photocatalytic activity is maintained under moderate compressive strains (−6% to −8%) and tensile strains below 4%. Moreover, the $Ga_2Ge_2S_3Se_3$ monolayer demonstrates the capability to initiate the oxygen evolution reaction (OER) under light irradiation, releasing electrons and protons (H^+) for the hydrogen evolution reaction (HER) to occur at low overpotential. The $Ga_2Ge_2S_3Se_3$ monolayer, even with a moderate solar-to-hydrogen efficiency of 14.80%, holds significant potential as a photocatalyst for water splitting, particularly when considering its other advantageous properties.

Data availability

The data that support the findings of this study are available from the corresponding author upon reasonable request.

Conflicts of interest

There are no conflicts of interest to declare.

References

1 R. Li, Y. Weng, X. Zhou, X. Wang, Y. Mi, R. Chong, H. Han and C. Li, *Energy Environ. Sci.*, 2015, **8**, 2377–2382.
2 Y. Li, C. Liao and S. C. Tjong, *Int. J. Mol. Sci.*, 2020, **21**, 8836.
3 N. Arif, M. N. Zafar, M. Batool, M. Humayun, M. A. Iqbal, M. Younis, L. Li, K. Li and Y.-J. Zeng, *J. Mater. Chem. C*, 2024, **12**, 12653–12691.
4 Z. Chang, J. Zhang, W. Dong, X. Meng, H. Wang, D. Wei and Y. Ren, *RSC Adv.*, 2020, **10**, 37820–37825.
5 H. Yu, X. Huang, P. Wang and J. Yu, *J. Phys. Chem. C*, 2016, **120**, 3722–3730.
6 M. Jothibas, S. Johnson Jeyakumar, C. Manoharan, I. Kartharinal Punithavathy, P. Praveen and J. Prince Richard, *J. Mater. Sci.: Mater. Electron.*, 2017, **28**, 1889–1894.
7 J. Pan, X. Shao, X. Xu, J. Zhong, J. Hu and L. Ma, *J. Phys. Chem. C*, 2020, **124**, 6580–6587.
8 D. Bhanderi, P. Lakhani and C. K. Modi, *RSC Sustainability*, 2024, **2**, 265–287.
9 P. Gomez-Romero, A. Pokhriyal, D. Rueda-García, L. N. Bengoa and R. M. González-Gil, *Chem. Mater.*, 2023, **36**, 8–27.
10 V. Kumar, G. Prasad Singh, M. Kumar, A. Kumar, P. Singh, A. K. Ansu, A. Sharma, T. Alam, A. S. Yadav and D. Dobrotă, *ACS Omega*, 2024, **9**, 6147–6164.
11 W. Xu, R. Wang, B. Zheng, X. Wu and H. Xu, *J. Phys. Chem. Lett.*, 2019, **10**, 6061–6066.
12 P. Ganguly, S. Mathew, L. Clarizia, S. Kumar R, A. Akande, S. J. Hinder, A. Breen and S. C. Pillai, *ACS Omega*, 2019, **5**, 406–421.
13 M. M. Khan and A. Rahman, *Catalysts*, 2022, **12**, 1338.
14 M. A. Susner, M. Chyasnavichyus, M. A. McGuire, P. Ganesh and P. Maksymovych, *Adv. Mater.*, 2017, **29**, 1602852.
15 F. Wang, T. A. Shifa, P. Yu, P. He, Y. Liu, F. Wang, Z. Wang, X. Zhan, X. Lou, F. Xia, *et al.*, *Adv. Funct. Mater.*, 2018, **28**, 1802151.
16 R. Samal, G. Sanyal, B. Chakraborty and C. S. Rout, *J. Mater. Chem. A*, 2021, **9**, 2560–2591.
17 Y. Dedkov, M. Yan and E. Voloshina, *Chem. Phys. Lett.*, 2020, **754**, 137627.
18 Z. Cheng, T. A. Shifa, F. Wang, Y. Gao, P. He, K. Zhang, C. Jiang, Q. Liu and J. He, *Adv. Mater.*, 2018, **30**, 1707433.
19 V. Kumar, K. Rajput and D. R. Roy, *Carbon*, 2021, **172**, 791–803.
20 M. Naseri, D. R. Salahub, T. V. Vu and H. Zakaryae, *J. Mater. Chem. C*, 2022, **10**, 11412–11423.
21 A. Jalil, S. Z. Ilyas, S. Agathopoulos, A. Qureshi, I. Ahmed and T. Zhao, *Appl. Surf. Sci.*, 2021, **565**, 150588.
22 P. D. Trung and H. D. Tong, *RSC Adv.*, 2024, **14**, 15979–15986.
23 A.-Y. Lu, H. Zhu, J. Xiao, C.-P. Chuu, Y. Han, M.-H. Chiu, C.-C. Cheng, C.-W. Yang, K.-H. Wei, Y. Yang, *et al.*, *Nat. Nanotechnol.*, 2017, **12**, 744–749.
24 Z. Feng, Y. Huang, S. Lin, H. Yuan and H. Chen, *J. Chem. Phys.*, 2023, **159**, 044115.
25 P. Giannozzi, S. Baroni, N. Bonini, M. Calandra, R. Car, C. Cavazzoni, D. Ceresoli, G. L. Chiarotti, M. Cococcioni and I. Dabo, *J. Phys.:Condens. Matter*, 2009, **21**, 395502.
26 J. P. Perdew, K. Burke and M. Ernzerhof, *Phys. Rev. Lett.*, 1997, **78**, 1396.

27 J. Heyd, G. E. Scuseria and M. Ernzerhof, *J. Chem. Phys.*, 2003, **118**, 8207–8215.
28 G. Kresse and D. Joubert, *Phys. Rev. B:Condens. Matter Mater. Phys.*, 1999, **59**, 1758.
29 S. Grimme, *J. Comput. Chem.*, 2006, **27**, 1787–1799.
30 A. Togo, L. Chaput and I. Tanaka, *Phys. Rev. B:Condens. Matter Mater. Phys.*, 2015, **91**, 094306.
31 J. Bardeen and W. Shockley, *Phys. Rev.*, 1950, **80**, 72.
32 T. V. Vu, A. Kartamyshev, M. D. Nguyen, K. D. Pham, T. T. Trinh, N. P. Nhuan and N. D. Hien, *Mater. Sci. Semicond. Process.*, 2024, **181**, 108590.
33 F. A. Rasmussen and K. S. Thygesen, *J. Phys. Chem. C*, 2015, **119**, 13169–13183.
34 I. Khan and J. Hong, *Nanotechnology*, 2020, **31**, 195704.
35 M. K. Mohanta and A. De Sarkar, *ACS Appl. Mater. Interfaces*, 2020, **12**, 18123–18137.
36 Y. Guo, S. Zhou, Y. Bai and J. Zhao, *Appl. Phys. Lett.*, 2017, **110**, 163102.
37 M. Born and K. Huang, *Dynamical Theory of Crystal Lattices*, Oxford University Press, 1996.
38 E. Cadelano, P. L. Palla, S. Giordano and L. Colombo, *Phys. Rev. B:Condens. Matter Mater. Phys.*, 2010, **82**, 235414.
39 J. Guo, R. Peng, X. Zhang, Z. Xin, E. Wang, Y. Wu, C. Li, S. Fan, R. Shi and K. Liu, *Small*, 2023, **19**, 2300766.
40 P. V. Sarma, R. Nadarajan, R. Kumar, R. M. Patinharayil, N. Biju, S. Narayanan, G. Gao, C. S. Tiwary, M. Thalakulam, R. N. Kini, *et al.*, *2D Mater.*, 2022, **9**, 045004.
41 L.-C. Zhang, G. Qin, W.-Z. Fang, H.-J. Cui, Q.-R. Zheng, Q.-B. Yan and G. Su, *Sci. Rep.*, 2016, **6**, 19830.
42 L. Guo, H. Yan, Q. Moore, M. Buettner, J. Song, L. Li, P. T. Araujo and H.-T. Wang, *Nanoscale*, 2015, **7**, 11915–11921.
43 J. Tao, W. Shen, S. Wu, L. Liu, Z. Feng, C. Wang, C. Hu, P. Yao, H. Zhang, W. Pang, *et al.*, *ACS Nano*, 2015, **9**, 11362–11370.
44 A. Falin, Q. Cai, E. J. Santos, D. Scullion, D. Qian, R. Zhang, Z. Yang, S. Huang, K. Watanabe, T. Taniguchi, *et al.*, *Nat. Commun.*, 2017, **8**, 15815.
45 J. W. Christopher, M. Vutukuru, D. Lloyd, J. S. Bunch, B. B. Goldberg, D. J. Bishop and A. K. Swan, *J. Microelectromech. Syst.*, 2019, **28**, 254–263.
46 L. Yu, Q. Yan and A. Ruzsinszky, *Nat. Commun.*, 2017, **8**, 1–8.
47 H. Yi, P. Solís-Fernández, H. Hibino and H. Ago, *Nanoscale Adv.*, 2022, **4**, 3786–3792.
48 B. Dong, Z. Wang, N. T. Hung, A. R. Oganov, T. Yang, R. Saito and Z. Zhang, *Phys. Rev. Mater.*, 2019, **3**, 013405.
49 L. Zhang, Y. Zhao, Y. Liu and G. Gao, *Nanoscale*, 2023, **15**, 18910–18919.
50 L. Zhang, Y. Liu, M. Wu and G. Gao, *Adv. Funct. Mater.*, 2024, 2417857.
51 A. K. Geim and I. V. Grigorieva, *Nature*, 2013, **499**, 419–425.
52 M. Sledzinska, G. Jumbert, M. Placidi, A. Arrighi, P. Xiao, F. Alzina and C. M. Sotomayor Torres, *ACS Appl. Electron. Mater.*, 2020, **2**, 1169–1175.
53 A. K. Katiyar, A. T. Hoang, D. Xu, J. Hong, B. J. Kim, S. Ji and J.-H. Ahn, *Chem. Rev.*, 2023, **124**, 318–419.
54 L. Yang, Q. Fu, W. Wang, J. Huang, J. Huang, J. Zhang and B. Xiang, *Nanoscale*, 2015, **7**, 10490–10497.
55 C. Gao, X. Yang, M. Jiang, L. Chen, Z. Chen and C. V. Singh, *Phys. Chem. Chem. Phys.*, 2022, **24**, 4653–4665.
56 G. Wei, D. A. Czaplewski, E. J. Lenferink, T. K. Stanev, I. W. Jung and N. P. Stern, *Sci. Rep.*, 2017, **7**, 3324.
57 F. Zhou, Y. Liu, Z. Lai, M. Liao, Y. Zhou, Y. Huang and J. Zhu, *RSC Adv.*, 2018, **8**, 20477–20482.
58 A. Fujishima and K. Honda, *Nature*, 1972, **238**, 37–38.
59 M. K. Mohanta and P. Jena, *J. Mater. Chem. C*, 2024, **12**, 1888–1896.
60 D. Er, H. Ye, N. C. Frey, H. Kumar, J. Lou and V. B. Shenoy, *Nano Lett.*, 2018, **18**, 3943–3949.
61 M. C. Toroker, D. K. Kanan, N. Alidoust, L. Y. Isseroff, P. Liao and E. A. Carter, *Phys. Chem. Chem. Phys.*, 2011, **13**, 16644–16654.
62 Q.-W. He, J.-H. Wang, D.-Y. Zhu, D.-S. Tang, Z. Lv, F. Guo and X.-C. Wang, *Nano Lett.*, 2024, **24**, 8979–8987.
63 Z. Wang and G. Zhou, *J. Phys. Chem. C*, 2019, **124**, 167–174.
64 S. Singh, P. Anees, S. Chandra and T. K. Ghanty, *J. Phys. Chem. C*, 2022, **126**, 8436–8449.
65 Z. Liu, B. Wang and C. Cazorla, *ACS Sustain. Chem. Eng.*, 2022, **10**, 16924–16934.
66 X.-H. Li, B.-J. Wang, X.-L. Cai, W.-Y. Yu, L.-W. Zhang, G.-D. Wang and S.-H. Ke, *RSC Adv.*, 2017, **7**, 44394–44400.
67 L. Ju, J. Shang, X. Tang and L. Kou, *J. Am. Chem. Soc.*, 2019, **142**, 1492–1500.
68 N. Vonrüti and U. Aschauer, *Phys. Rev. Mater.*, 2018, **2**, 105401.
69 M. Pandey, C. Pandey, R. Ahuja and R. Kumar, *Nano Energy*, 2023, **109**, 108278.
70 L.-B. Shi, S. Cao and M. Yang, *Phys. E*, 2019, **107**, 124–130.
71 R. Roldán, A. Castellanos-Gomez, E. Cappelluti and F. Guinea, *J. Phys.: Condens. Matter*, 2015, **27**, 313201.
72 Y. Jiao, F. Ma, G. Gao, J. Bell, T. Frauenheim and A. Du, *J. Phys. Chem. Lett.*, 2015, **6**, 2682–2687.
73 X. Zhang, X. Zhang, P. M. Ajayan, J. Wen and H. D. Espinosa, *Small*, 2022, **18**, 2105194.
74 E. Blundo, E. Cappelluti, M. Felici, G. Pettinari and A. Polimeni, *Appl. Phys. Rev.*, 2021, **8**, 021318.
75 X. Peng, Q. Wei and A. Copple, *Phys. Rev. B:Condens. Matter Mater. Phys.*, 2014, **90**, 085402.
76 D. D. Vo, T. V. Vu, A. Kartamyshev, T. H. Ho and N. N. Hieu, *Nanoscale Adv.*, 2024, **6**, 6019–6028.
77 J. K. Nørskov, T. Bligaard, A. Logadottir, J. Kitchin, J. G. Chen, S. Pandelov and U. Stimming, *J. Electrochem. Soc.*, 2005, **152**, J23.
78 C. Quan, S. Ji, R. Yao, W. Liu, J. Yang and X. Li, *Int. J. Hydrogen Energy*, 2024, **56**, 1227–1234.
79 T. V. Vu, N. N. Hieu, D. D. Vo, A. Kartamyshev, H. D. Tong, T. T. Trinh, V. Khuong Dien, Z. Haman, P. Dey and N. Khossossi, *J. Phys. Chem. C*, 2024, **128**, 4245–4257.
80 L. Ju, M. Bie, X. Tang, J. Shang and L. Kou, *ACS Appl. Mater. Interfaces*, 2020, **12**, 29335–29343.
81 Y. Sun, A. Huang and Z. Wang, *RSC Adv.*, 2019, **9**, 26321–26326.

82 Q. Cai, W. Hong, C. Jian, X. He and W. Liu, *Adv. Energy Sustainability Res.*, 2023, **4**, 2200178.
83 D. W. Boukhvalov, S. Nappini, M. Vorokhta, T. O. Menteş, L. Piliai, M. Panahi, F. Genuzio, J. De Santis, C.-N. Kuo, C. S. Lue, *et al.*, *Adv. Funct. Mater.*, 2021, **31**, 2106228.
84 Y. Chen, X. Fu and Z. Peng, *Metals*, 2023, **13**, 1163.
85 L. M. Herz, *ACS Energy Lett.*, 2017, **2**, 1539–1548.
86 D. Shi, V. Adinolfi, R. Comin, M. Yuan, E. Alarousu, A. Buin, Y. Chen, S. Hoogland, A. Rothenberger, K. Katsiev, *et al.*, *Science*, 2015, **347**, 519–522.
87 Y. Cai, G. Zhang and Y.-W. Zhang, *J. Am. Chem. Soc.*, 2014, **136**, 6269–6275.
88 Y. Wang, Y. Li and Z. Chen, *J. Mater. Chem. C*, 2015, **3**, 9603–9608.
89 C. Long, Y. Liang, H. Jin, B. Huang and Y. Dai, *ACS Appl. Energy Mater.*, 2018, **2**, 513–520.
90 Y. Jing, Z. Zhou, J. Zhang, C. Huang, Y. Li and F. Wang, *Phys. Chem. Chem. Phys.*, 2019, **21**, 21064–21069.
91 X. Liu, Z. Zhang, Z. Ding, B. Lv, Z. Luo, J.-S. Wang and Z. Gao, *Appl. Surf. Sci.*, 2021, **542**, 148665.
92 X. Liu, W. Kang, J. Zhao, Y. Wang, W. Wang, L. Wang, L. Fang, Q. Chen and M. Zhou, *Phys. Status Solidi RRL*, 2022, **16**, 2100417.
93 P. Jamdagni, A. Kumar, S. Srivastava, R. Pandey and K. Tankeshwar, *Phys. Chem. Chem. Phys.*, 2022, **24**, 22289–22297.
94 K. Chaoui, W. Elaggoune and K. Zanat, *Int. J. Hydrogen Energy*, 2024, **91**, 1221–1231.